SUPPLEMENTARY INFORMATION

Supplementary Methods: Database Compilation

Nature of the indicators and depositional ranges. The sea level indicators take a variety of forms, including: constructional coral terraces that provide both geomorphological and ecological information; coral biofacies in limestones that provide ecological but not geomorphological information; erosional features such as wave-cut terraces, sea caves, bioerosional notches, and raised beaches; and sedimentological and biofacial indicators of depositional depth.

Most of the indicators reflect deposition or formation within a specific range of depths. The most common reef terraces and associated coral assemblages, for instance, are generally interpreted as indicating deposition between mean low tide level and 5 m below mean low tide level [1,2]. Intertidal sedimentary facies indicate deposition within the tidal range. While recognizing that LIG tidal amplitudes could have been slightly different than today, we convert descriptive ranges such as these into a common reference frame based on the tidal ranges reported in tide tables at a nearby modern locality. We also attempt to correct for variability in the measurement datum; while most sea level indicators have altitudes reported with respect to "modern sea level", some are more usefully described with reference to datums such as the mean low tide level or mean high tide level. We convert such datums into a mean tide level datum.

Some data, such as subtidal sedimentary facies, are limiting points; they place an upper or lower limit on past sea level but do not indicate a specific depositional depth. In statistical terminology, limiting points are censored data.

Age. Age constraints on our data come from a variety of sources with a range of precisions. In some cases, age is constrained only by stratigraphic relationships with other units. In many cases, particularly involving coral reefs, radiometric (U/Th) dates are available. Other age constraints are derived from amino acid racemization, electron spin resonance dating, and related techniques such as thermoluminescence.

In three cases (the global oxygen isotope curve, the Red Sea oxygen isotope curve, and the Dutch sea level curve), relative ages are known with more precision than absolute ones. As described below, we

have scaled and shifted the age models of the Red Sea and Dutch local sea level curves to be consistent with the Lisiecki and Raymo[3] age model for the global oxygen isotope curve. All of the dates outputted by our analysis should therefore be viewed within the context of this age model, which places the start of the Penultimate Termination at 135 ka and the peak of the Last Interglacial at about 122–126 ka.

When only a single conventional U/Th measurement from a unit is available, we expand the quoted ranges by 350%, following the empirical observation of Scholz et al.[4] of the overestimate of the precision of ages from single-sample measurements. When multiple measurements are reported, we employ their inverse-variance weighted mean. We expand the inverse-variance weighted standard deviation using a Student's t-distribution so that the 95% confidence interval spans $\pm 1.96\sigma$, with σ the standard deviation, as in a Gaussian distribution.

Tectonic uplift or thermal subsidence rate. In order to remove the local tectonic contribution to paleo-sea level, we seek locally calibrated subsidence or uplift estimates for each locality. For most of the points in our database, no estimate of uplift or subsidence is available, but the value is expected to be near zero for short ($\sim$ 100 ky) time scales. For these locations, we adopt an estimate of 0 ± 1 cm/ky. (For subsiding localities, this is conservative with regards to peak sea level, as underestimates of subsidence will lead to sea level underestimates.) In a few regions where estimates are available, including much of the Bahamas and Hawai'i, subsidence or uplift is on the order of 1–2 cm/ky. A few localities have exhibited uplift (Barbados, Patagonia, southern England) or subsidence (the Netherlands, Pacific and Indian Ocean atolls) in excess of about 10 cm/ky. The fastest uplifting locality in our database, Barbados, is rising at about 28 cm/ky.

Coverage. Our database attains fairly good geographic coverage, including the northwestern, northeastern, and southwestern Atlantic coasts; the Carribean; Alaska, Greenland, Svalbard, and Siberia; Australia; the southwestern Indian coast; and Pacific and Indian Ocean islands (Figures 1 and 3; Table S1). Where nearby localities subject to less uplift are available, we have tried to limit the amount of data from rapidly uplifting sites, though we include Barbados because of its prominence in the literature. However, given the long history of the geological study of Pleistocene sea level indicators , which began not long after the collapse of the Diluvian hypothesis in the early nineteenth century[5], we do not claim that our database comprehensively represents the entire literature.

Supplementary Methods: Database

The database is recorded in a spreadsheet that accompanies this Supplementary Information. Two of the sites are re-analyses of data available elsewhere that require special explanations: the re-aligned Red Sea sea level curve of Rohling et al.[6] and a subsidence-corrected Dutch sea level curve based on the work of Zagwijn[7].

Red Sea. The Red Sea record is a planktonic foraminiferal oxygen isotope record that, because of the hydrological structure of the sea[8], is essentially a record of local sea level at the strait of Bab-el-Mandeb. The oxygen isotopic composition of Red Sea water is controlled primarily by evaporation. Water exchange between the Red Sea and the Indian Ocean occurs through the strait; when sea level is lower, water exchange decreases, which increases the residence time of water in the Red Sea and thus yields heavier oxygen isotope values. This greatly magnifies the isotopic effects of sea level change. The difference between the modern and the Last Glacial Maximum in the Red Sea is nearly 6‰, whereas in the open ocean the difference is approximately 1.8‰.

Using a hydrological model, Rohling et al.[6] constructed a sea level record with a raw 1σ precision of 6 m for the Last Interglacial from two Red Sea cores sampled for oxygen isotopes at 10 cm resolution. They aligned their record temporally with the record derived from U/Th-dated Barbados coral data[9]; in this age model, their record has a temporal resolution of 200–400 years. It indicates that local sea level rose to at least 6 ± 3.5 m, and perhaps as high as 11 m, during the peak interglacial.

We have for consistency realigned the Red Sea curve against the age model for the global oxygen isotope stack[3], which is based primarily on alignment against the GRIP ice core. This realignment required shifting the curve earlier by 2.4 ka and expanding the duration between measurements 1.2 times. We include in our database the re-aligned sea level curve derived from the KL11 core, which Rohling et al. argue provides a higher resolution record than the KL09 core.

Netherlands. The Dutch Eemian sea level record of Zagwijn[7] is based on sedimentological and micropaleontological data from numerous cores through the Amsterdam and Amersfoort basins, as well as cores along

the Noord-Holland coast, in Friesland, and in the North Sea. Sea level indicators in these cores are provided by facies transitions representing, for example, the infiltration of marine water into a freshwater lake or the maximum elevation of clays deposited in a salt-marsh environment. Relative age constraints are provided by characteristic Eemian pollen zones, many of which have durations established to fairly high precision based upon the counting of varves in an annually-layered lacustrine diatomite in northwestern Germany[10]. We place peak sea level in the middle third of zone E5 based upon the position of the maximum flooding interval within the more recent Amsterdam-Terminal borehole[11]. We estimate absolute ages from these relative ages by aligning the sea level curve against the global oxygen isotope stack.

Zagwijn reported sea level estimates without correction for long-term isostasy, compaction, or tectonics. To correct for these factors, we use the backstripping-derived Quaternary rate estimates of Kooi et al.[12]. These vary considerably across the Netherlands and the North Sea, ranging from about 12 cm/ky in Amersfoort to about 18 cm/ky in Petten. Thus adjusted, Zagwijn's data indicate that a maximum local sea level of about 5 ± 2 m was attained in the Netherlands for much of the Last Interglacial.

Supplementary Methods: Statistical Model

Preliminaries and Notation. The ultimate goal of our statistical analysis is to determine the posterior probability distribution of sea level through time, conditioned upon the measurements in our database. Expressed symbolically, our aim is to evaluate the probability $P(f(\mathbf{x}, g)|\mathbf{r}, \mathbf{z}, \mathbf{t}, \mathbf{D}, \mathbf{u})$ for locations $\mathbf{x}$ on Earth's surface and times g, where f represents the true value of sea level at $\mathbf{x}$ and g. In our database, each sea level indicator is assigned an index $i = 1, \ldots, N$ and is characterized by

$\mathbf{r}_i$, its exact geographic position,

z_i, a noisy measurement of its altitude,

t_i, a noisy measurement of its age,

$\mathbf{D}_i$, a closed or open interval reflecting its depositional range, and

u_i, a noisy estimate of the long-term average uplift or subsidence rate.

maximum elevation of clays deposited in a salt-marsh environment. Relative age constraints are provided by characteristic Eemian pollen zones, many of which have durations established to fairly high precision based upon the counting of varves in an annually-layered lacustrine diatomite in northwestern Germany[10]. We place peak sea level in the middle third of zone E5 based upon the position of the maximum flooding interval within the more recent Amsterdam-Terminal borehole[11]. We estimate absolute ages from these relative ages by aligning the sea level curve against the global oxygen isotope stack.

Zagwijn reported sea level estimates without correction for long-term isostasy, compaction, or tectonics. To correct for these factors, we use the backstripping-derived Quaternary rate estimates of Kooi et al.[12]. These vary considerably across the Netherlands and the North Sea, ranging from about 12 cm/ky in Amersfoort to about 18 cm/ky in Petten. Thus adjusted, Zagwijn's data indicate that a maximum local sea level of about 5 ± 2 m was attained in the Netherlands for much of the Last Interglacial.

Supplementary Methods: Statistical Model

Preliminaries and Notation. The ultimate goal of our statistical analysis is to determine the posterior probability distribution of sea level through time, conditioned upon the measurements in our database. Expressed symbolically, our aim is to evaluate the probability $P(f(\mathbf{x}, g)|\mathbf{r}, \mathbf{z}, \mathbf{t}, \mathbf{D}, \mathbf{u})$ for locations $\mathbf{x}$ on Earth's surface and times g, where f represents the true value of sea level at $\mathbf{x}$ and g. In our database, each sea level indicator is assigned an index $i = 1, \ldots, N$ and is characterized by

$\mathbf{r}_i$, its exact geographic position,

z_i, a noisy measurement of its altitude,

t_i, a noisy measurement of its age,

$\mathbf{D}_i$, a closed or open interval reflecting its depositional range, and

u_i, a noisy estimate of the long-term average uplift or subsidence rate.

When $\mathbf{D}_i$ is a closed interval, we replace it with d_i, a Gaussian estimate of depositional depth characterized by the same mean and variance as the uniform distribution on $\mathbf{D}_i$, as discussed in the Methods section.

We collect these parameters into vectors $\mathbf{r}$, $\mathbf{z}$, $\mathbf{t}$, $\mathbf{D}$, $\mathbf{u}$, and $\mathbf{d}$. Similarly, we collect what will be the true sea levels in a vector $\mathbf{f}$ evaluated at the times $\mathbf{g}$ and locations $\mathbf{x}$, whose elements f_j, g_j and $\mathbf{x}_j$ for $j = 1, \ldots, M$ are the desired sea levels and evaluation points. Only when geographical positions and depositional ranges are concerned does the bold vector notation serve double-duty: $\mathbf{x}$ and $\mathbf{r}$ are either coordinates or vectors of coordinates, and $\mathbf{x}_i$, $\mathbf{r}_i$ and $\mathbf{x}_j$, $\mathbf{r}_j$ are individual sets of coordinates. Likewise, $\mathbf{D}$ is either a depositional range or an array of depositional ranges, and $\mathbf{D}_i$ is an individual depositional range. This dual purpose is not, however, likely to lead to confusion.

Gaussian process regression. We proceed from this point using a Gaussian process approach[13]. We must select some covariance function for true sea level, $k(\mathbf{r}_i, g_i; \mathbf{r}_j, g_j)$, as we will address below. Let $(\mathbf{f}, \mathbf{g})$ refer to the vectors of true sea levels and ages that correspond to the vectors of measurements $(\mathbf{z}, \mathbf{t}, \mathbf{D}, \mathbf{u})$; i.e., with every entry (f_i, g_i), we associate an entry $(z_i, t_i, \mathbf{D}_i, u_i)$ for all indices $i = 1, \ldots, N$. With the covariance function k given, we can then readily recover an estimate of true sea level at any arbitrary location $\mathbf{x}'$ and time g' through straight-forward kriging interpolation[14]. We denote the mean and variance of this estimate by $\overline{f}(\mathbf{x}', g')$ and $\mathbf{V}(f(\mathbf{x}', g'))$, respectively.

As before, the vectors $\overline{\mathbf{f}}$, $\mathbf{x}'$ and $\mathbf{g}'$ will collect the mean estimates of the sea levels at the desired points $\mathbf{x}'$ and $\mathbf{g}'$ in space and time. The sets of desired evaluation points $(\mathbf{x}'_j, g'_j)$, $j = 1, ..., M$, and the measurements $(\mathbf{r}_i, g_i)$, $i = 1, ..., N$ need not necessarily overlap. The matrix $\mathbf{V}''$ collects the kriging (co)variance of $\mathbf{f}'$ at and between $(\mathbf{x}', \mathbf{g}')$. Let $\mathbf{K}$, $\mathbf{K}'$, and $\mathbf{K}''$ be the covariances of $(\mathbf{f}, \mathbf{g})$ and/or $(\mathbf{f}', \mathbf{g}')$ at the observed and desired points, i.e., let the symmetric square matrices $\mathbf{K}$ and $\mathbf{K}''$ and the rectangular matrix $\mathbf{K}'$ be defined by their elements:

$$K_{ij} = k(\mathbf{r}_i, g_i; \mathbf{r}_j, g_j) \qquad \text{where } i, j = 1, ..., N, \tag{S1}$$

$$K''_{ij} = k(\mathbf{x}'_i, g'_i; \mathbf{x}'_j, g'_j) \qquad \text{where } i, j = 1, ..., M, \tag{S2}$$

$$K'_{ij} = k(\mathbf{r}_i, g_i; \mathbf{x}'_j, g'_j) \qquad \text{where } i = 1, ..., N \text{ and } j = 1, ..., M. \tag{S3}$$

From this, the kriging step consists of calculating $\bar{\mathbf{f}}$, the $M \times 1$ vector of mean sea level estimates at $(\mathbf{x}', \mathbf{g}')$, as

$$\bar{\mathbf{f}} = \mathbf{K}'^{\top}\mathbf{K}^{-1}\mathbf{f}, \tag{S4}$$

which has

$$\mathbf{V}'' = \mathbf{K}'' - \mathbf{K}'^{\top}\mathbf{K}^{-1}\mathbf{K}' \tag{S5}$$

as its $M \times M$ covariance matrix. It is clear from the above that, when $\mathbf{x}' = \mathbf{r}$ and $\mathbf{g}' = \mathbf{g}$, $\mathbf{K} = \mathbf{K}' = \mathbf{K}''$, and therefore $\bar{\mathbf{f}} = \mathbf{f}$ and $\mathbf{V}'' = \mathbf{0}$. In other words, when the queried points are identical to the measurement locations, the interpolated values of true sea level remain unchanged and receive no kriging variance.

We can therefore replace the problem of finding the posterior probability of sea level anywhere, $P(f(\mathbf{x}, g)|\mathbf{r}, \mathbf{z}, \mathbf{t}, \mathbf{D}, \mathbf{u})$, with the more tractable problem of finding $P(\mathbf{f}, \mathbf{g}|\mathbf{z}, \mathbf{t}, \mathbf{D}, \mathbf{u})$, which is the posterior probability of sea level at the smaller set of points defined by the measurement locations. After adjusting altitude z_i for uplift or subsidence rate u_i over a time g_i, we define the corrected altitude z'_i as

$$z'_i \equiv z_i - g_i u_i, \tag{S6}$$

with variance

$$\sigma^2_{z'i} \equiv \sigma^2_{zi} + g_i^2 \sigma^2_{ui}, \tag{S7}$$

and we define the sea level measurement s_i and its variance σ^2_{si} as

$$s_i \equiv z'_i - d_i, \tag{S8}$$

$$\sigma^2_{si} \equiv \sigma^2_{z'i} + \sigma^2_{di}, \tag{S9}$$

where σ^2_{zi}, σ^2_{ui}, and σ^2_{di} are the variances respectively of altitude z_i, uplift rate u_i, and depositional depth d_i. By Bayes' theorem,

$$P(\mathbf{f}, \mathbf{g}|\mathbf{s}, \mathbf{t}) \propto P(\mathbf{s}, \mathbf{t}|\mathbf{f}, \mathbf{g}) \cdot P(\mathbf{f}, \mathbf{g}). \tag{S10}$$

We drop the position variable $\mathbf{r}$ from the notation, since its values are fixed in the data set and implicit in the indexing of the other variables. For uncensored sea level measurements, we have the likelihood

$$P(s_i|f_i, g_i) \sim \mathcal{N}(f_i, \sigma^2_{si}). \tag{S11}$$

In other words, the probability of observing sea level s_i at a point in the data set that has a true sea level of f_i is given by a Gaussian centered on the truth with variance σ^2_{si}. For censored data,

$$P(s_i|f_i, g_i) \sim \mathcal{N}(f_i, \sigma^2_{si}) \cdot \delta\big((z'_i - s_i) \in \mathbf{D}_i\big) \tag{S12}$$

where δ is an indicator function that is 1 when $z'_i - s_i$ is in the depositional range $\mathbf{D_i}$ and 0 otherwise. For instance, if $\mathbf{D}_i$ is $(-\infty, -2]$, reflecting deposition at least two meters below mean tide level, then δ would be 1 for $s_i \geqslant z'_i + 2$ and 0 otherwise. For age measurements, we have the likelihood

$$P(t_i|g_i) \sim \mathcal{N}(g_i, \sigma^2_{ti}), \tag{S13}$$

where σ_{ti}^2 is the variance of age measurement t_i. For the sea level vector $\mathbf{f}$, we compute a prior of the form

$$P(\mathbf{f}|\mathbf{g}) \sim \mathcal{N}(\mu(\mathbf{g}), \mathbf{K}(\mathbf{g})), \tag{S14}$$

as discussed below, where we use the notation $\mu(\mathbf{g})$ and $\mathbf{K}(\mathbf{g})$ for the covariance to emphasize the dependence of the mean and covariance not just on locations $\mathbf{r}$ but also on ages $\mathbf{g}$. For the age vector $\mathbf{g}$ itself, we assume a uniform prior.

Prior distribution for sea level and ice volume. The prior distribution for sea level and ice volume is based upon the global oxygen isotope curve of ref. 3 and is determined through a five step process. First, we construct a multivariate Gaussian distribution for total global ice volume through time based upon the oxygen isotope curve. Second, we construct a distribution for the volume of each major ice sheet and Northern and Southern Hemisphere glaciers conditioned upon total global ice volume. Third, we sample 250 alternative ice sheet histories from these distributions and use a physical model to determine the associated local sea levels. Fourth, we add a thermosteric component of sea level to each alternative history. Finally, we compute the mean and covariance of local sea level, global sea level, and ice sheet volumes as a function of space and time from these alternative histories. The spatial covariance of local sea level with global sea level at two illustrative time points and the temporal covariance of global sea level are shown in Figures S4 and S5.

Distribution of global ice volume over time. The distribution of global ice volume over time is based upon the global oxygen isotope curve of ref. 3. First, we note that the difference in δ^{18}O between the present value ($\delta_0 = 3.23 \pm 0.03‰$) and the peak Last Glacial Maximum ($5.02 \pm 0.03‰$ at 18 ka) is $1.79 \pm 0.04‰$ and is associated with a change in sea level of about 125 m (ref. 15). Assuming a simple linear relationship between δ^{18}O and global ice volume yields a proportionality constant c of about 70 m/‰. Ref. 16 notes, however, that there is considerable deviation from a simple linear relationship; their results indicate that this assumption can give rise to an inaccuracy of as much as 20 m. We therefore assume that global ice volumes

derived from this scaling factor have a 1σ uncertainty of ± 10 m in addition to any uncertainty arising from measurement imprecision. From this relationship, we derive mean predictions for total global ice volume and the diagonal terms of the associated covariance matrix: at time i, where $\Delta_i = \delta_i - \delta_0$, the mean ice volume prediction $\overline{I_i} = c\Delta_i$ and its variance $\sigma^2_{I_i} = c^2\sigma^2_{\Delta_i} + 100$.

To determine the off-diagonal terms, we note that changes in global ice volume are constrained by changes in the global oxygen isotope curve: $I_i - I_j = (c \pm \sigma_c)(\delta_i - \delta_j)$ where $I_{i,j}$ are global ice volumes at times i and j, c is the proportionality constant between global ice volume and oxygen isotope values, σ_c is the standard deviation of c, and $\delta_{i,j}$ are the values of the oxygen isotope curve at times i and j. As noted previously, we use $c = 70$ m/‰, but also note that at values of δ close to the present value, the proportionality constant can vary by as much as about 70%[16]. We therefore use σ_c = 25 m/‰. The covariance of I_i and I_j is given by $0.5 \times (\sigma^2_{I_i} + \sigma^2_{I_j} - \sigma^2_{I_i - I_j})$, where $\sigma^2_{I_i - I_j} = \sigma^2_c(\Delta_i - \Delta_j)^2 + c^2(\sigma^2_{\Delta_i} + \sigma^2_{\Delta_j})$.

Because c changes over time, we apply a Gaussian taper with a standard deviation of 3 ka to the covariance. The covariance between global ice volume at times i and j is thus given by $c_I(i,j) = 0.5 \times e^{-\left(\frac{i-j}{5}\right)^2} \times (\sigma^2_{I_i} + \sigma^2_{I_j} - \sigma^2_{I_i - I_j})$. (The resulting distribution is shown in Figures S1 and S2.)

Distribution of ice sheet volumes conditional upon global ice volume. To determine the distribution of ice sheet volumes conditional upon global ice volume, we start with two alternative reconstructions of LGM-to-present ice sheet volumes[15], distinguishing between five ice sheets – Laurentide, Scandinavian, Greenland, West Antarctic and East Antarctic – as well as northern and southern hemisphere glaciers. From each base model, we generate approximately 8000 random perturbations by multiplying the change in each ice sheet's volume between each time step by a random log normal factor with a log standard deviation of $3\times$. We similarly multiply the change in total ice volume between each time step by a random log normal factor with a log standard deviation of $1.5\times$ and then multiply the ice sheet volumes by a correction factor that maintains the proportional distribution of ice volume among the ice sheets while ensuring that ice volumes add to the correct value. We also add cases with additional mass loss from the ice sheets, in

which total ice volume shrinks below its present value. We then bin by total ice volume to generate the desired distribution (Figure S3). Note that this distribution is a function of global ice volume, not of time. When sampling ice sheet volume over time, we impose a weak constraint on the rate of change of ice sheet volumes so as to prevent wild oscillations in ice distribution during intervals of little change in total ice volume. To turn a numerical quantity reflecting the total volume in ice sheet into a geographical map of land ice, we scale the map from the timeslice of the ICE-5G LGM-to-present reconstruction[15] that is closest to but not smaller than the desired volume.

Alternative histories for physical modeling. We draw 250 samples from the distribution for global ice volume. To account for uncertainty in the dating of the global oxygen isotope curve, we keep one time point (120 ka) fixed as an anchor for our age model and allow the nominal 1-ky spacing between oxygen isotope measurements to vary with a standard deviation of 250 y. We then interpolate to get evenly spaced measurements and subsequently draw associated ice sheet histories from the distribution described above. The 250 alternative histories thus calculated serve as inputs to the physical model described in the Methods section, which is based on the gravitationally self-consistent sea-level equation derived by Mitrovica et al.[17] and calculates local sea levels for each history.

For each history, we also estimate an associated thermosteric change in sea level. Based upon the projections for year 3000 thermal expansion summarized by ref. 18, we estimate a relationship between temperature and thermosteric sea level of about 0.39 ± 0.14 m/°C. Assuming that the ~ 125 m equivalent sea level of global ice volume change between the LGM and present was associated with ~ 5°C of cooling yields about -1.55 ± 0.57 cm of thermal contracting per meter ice volume growth. To allow the thermosteric component of sea level to change without much accompanying ice volume change, we add an additional ice volume-independent thermosteric term with a mean of zero, a standard deviation of 2 m, and a Gaussian temporal covariance with a standard deviation of 2 ky (Figure S2).

We explicitly calculate the mean and covariance for sea level and ice volume over time from these

alternative histories, which we then store as a lookup table. We use linear interpolation over time to provide continuity. For computational efficiency, we perform these operations using a principal component decomposition of sea level and retain sufficient principal components to account for 99% of the variance. This reduces an computationally nearly intractable 71,350 x 71,350 covariance matrix to an easily tractable 177 x 177 covariance matrix. For time points that fall outside the principal time range of interest (149–100 ka), we use a spatial mean and covariance that combines results across all time points.

Temporal taper function. To reducing sampling-associated noise in the covariance function, we employ a Gaussian temporal taper function as described in the Methods section. We tested four different values for the standard deviation τ of this taper function: 2 ky, 3 ky, 4 ky, and ∞ (i.e., no taper). The resulting GSL projections are shown in Figure S9 and summary statistics are shown, alongside summary statistics for different data subsets, in Table S2. We adopted a 3 ky taper for the main analysis.

Algorithm for sampling the posterior sea level distribution. To explore the distribution in equation S10, we use a three-step Gibbs sampler that in turn calculates $p(s|g)$, $p(f|s,g)$ and $p(g|f)$. We start by initializing $\mathbf{g} = \mathbf{t}$ for all data points and $z'_i = z_i - g_i u_i$ and $f_i = s_i = z'_i - d_i$ for the uncensored ones. By simple kriging interpolation (equations S4 and S5), we estimate f_i at the remaining data points.

1. In step one of our algorithm, we calculate values of sea level measurements $\mathbf{s}$ from $\mathbf{z}$, $\mathbf{D}$, $\mathbf{g}$ and $\mathbf{u}$. For uncensored data, s_i is as defined in equation S8. For censored data, we sample s_i from the distribution in equation S12, with an additional variance term σ^2_{fi}, the kriging variance of f_i.

2. In step two, we update our estimate of true sea level $\mathbf{f}$ based upon the new $\mathbf{s}$ as follows. We define the matrix of the sea level measurement noise $\mathbf{N}$, with elements σ^2_{si} along the diagonal and zero elsewhere. Then, by Gaussian process regression, paralleling equation S4, we calculate

$$\mathbf{f} = \mathbf{K}(\mathbf{g})^\top (\mathbf{K}(\mathbf{g}) + \mathbf{N})^{-1} \mathbf{s}, \tag{S15}$$

the vector of sea level predictions and the vector of their variances

$$\mathbf{\Sigma} = \text{diag}\{\mathbf{K}(\mathbf{g})^\top(\mathbf{I} - (\mathbf{K}(\mathbf{g}) + \mathbf{N})^{-1}\mathbf{K}(\mathbf{g}))\}, \tag{S16}$$

where diag denotes the diagonal elements.

3. In step three, we update our estimate of the true ages $\mathbf{g}$. To do this, we follow a Markov Chain Monte Carlo approach applying the Metropolis-Hastings algorithm sequentially to each g_i. Let $\mathbf{g}_{-i}$ represent $\mathbf{g}$ with element i removed. For each i, we sample from the distribution $P(g_i|\mathbf{t}, \mathbf{g}_{-i}, \mathbf{f})$, which, by multiple applications of Bayes' theorem and the facts that $P(\mathbf{t}|\mathbf{g}) = \prod_i P(t_i|g_i)$ and that $P(\mathbf{t}|\mathbf{f}) = P(\mathbf{t})$, reduces as

$$P(g_i|\mathbf{t}, \mathbf{g}_{-i}, \mathbf{f}) \propto P(t_i|g_i) \cdot P(\mathbf{f}|\mathbf{g}) \cdot P(\mathbf{g}). \tag{S17}$$

The first term is given by equation S13, and the second term by equation S14. We can drop the third term because of our assumption of a uniform prior for $\mathbf{g}$.

We generate test values g_i' using a Gaussian function $q(g_i'; g_i)$ centered at g_i and bounded such that, when stratigraphic ordering is known, a point j that follows a point i always has $g_j \leqslant g_i$. (Where no bounds apply, $q(a; b) = q(b; a)$.) For the sequences where relative ages are known more precisely than absolute ones, these are calculated in terms of time after the preceding point. Following the Metropolis-Hastings algorithm[19], we accept a candidate g_i' with probability

$$\min\left(1, \frac{P(g_i'|\mathbf{t}, \mathbf{g}_{-i}, \mathbf{f}) \cdot q(g_i; g_i')}{P(g_i|\mathbf{t}, \mathbf{g}_{-i}, \mathbf{f}) \cdot q(g_i'; g_i)}\right) = \min\left(1, \frac{P(t_i|g_i') \cdot P(\mathbf{f}|\mathbf{g}_{-i}, g_i') \cdot q(g_i; g_i')}{P(t_i|g_i) \cdot P(\mathbf{f}|\mathbf{g}_{-i}, g_i) \cdot q(g_i'; g_i)}\right). \tag{S18}$$

So that we can assess results within a common temporal reference frame, we arbitrarily set the temporal variance σ_{ti}^2 for the first step of our longest quasi-continuous sequence of data points (the sea level curve derived from the global oxygen isotope stack, for most runs) to zero.

This algorithm, repeated a large number of times, samples the probability distribution described by equation S10. We thin the results by storing every 20th sample and account for burn-in by discarding the

first 50 stored samples. After several parallel executions of the algorithm, each of which store at least about 200 samples, we check for convergence by inspecting the autocorrelation of stored values of $\mathbf{g}$ and discard executions that appear not to converge. To generate our target distribution $P(f(\mathbf{x}, g)|\mathbf{s}, \mathbf{r}, \mathbf{t})$, we use kriging interpolation (equations S1–S5) to estimate the sea level field at all spatial and temporal points of interest for each stored sample.

We note that this algorithm, while satisfying from a theoretical perspective, could benefit from greater computational efficiency. The most time-consuming steps in its execution are the inversions of the covariance matrices, which for a database of n samples require $\mathcal{O}(n^3)$ operations. This inversion occurs once in step 2 and $n + 1$ times in step 3. Thus, each iteration of the algorithm is $\mathcal{O}(n^4)$. Repeating the algorithm a few thousand times in the courses of a Monte Carlo simulation with a database of about 100 points can therefore take a day or more; without increased efficiency, larger data sets will become unmanageable.

Summary statistics for outlier analysis. To identify outliers among the data points, we compute the *probability of a measurement* given the assessed sea level distribution. To do this, we take the average over all N stored MCMC iterations of the probability that the parameter f (local sea level, global sea level, or age) with measured value $f_m \pm \sigma_m$ was drawn from the distribution indicated by iteration i, with mean f_i and standard deviation σ_i. For indicative points, the probability for each iteration is given by a χ^2 distribution with one degree of freedom on the parameter $\frac{(f_i - f_m)^2}{\sigma_i^2 + \sigma_m^2}$. For limiting points, the probability is given by a cumulative normal distribution with mean $f_i - f_m$ and variance $\sigma_i^2 + \sigma_m^2$.

Pseudo-proxy validation analysis. To test our statistical model, we took 20 of the synthetic sea level histories used to generate the prior distribution and sampled them at the same points in space and time and with same chronological and sea-level errors as in the data set. The results show that the algorithm performs more than adequately the task of reconstruction global sea level, rates, and ice volumes (e.g., Figure S6). For these twenty synthetic histories, maximum GSL and GSL rates tend to be slightly higher than expected based on the exceedance values (Figure S7). For instance, while, as expected, in 19 of 20 cases peak GSL

exceeds the 95% exceedance value, in 15 of 20 cases it exceeds the 60% exceedance value (compared to the expected 12 of 20), and in 10 of 20 cases it exceeds the 30% exceedance value (compared to the expected 6 of 20). Given the small number of histories run, a consequence of the computational expense of each analysis, it is not possible to draw general conclusions from this slight apparent low bias.

Supplemental Discussion

Outlier analysis. To search for outliers, we estimated the posterior probabilities for each of our sea level measurements and age measurements given the distribution at each point for sea level and age projected by our statistical model. No data point was a strong outlier, but four sites generated sea level measurement probabilities between 0.10 and 0.33, and four generated age measurement probabilities between 0.11 and 0.30.

First, at Kahe Beach State Park, Oahu, Hawai'i, Hearty et al.[20] describe a marine conglomerate at 12 m above present sea level. Corrected for uplift of Oahu, this suggests a paleo-sea level of at least 9.6 ± 1.3 m. Our model instead assigns a sea level of 7.1 ± 1.5 m, raising the possibility that uplift has been greater than expected.

Second, our model identifies as an outlier early Weichselian (post-Eemian) lacustrine sediment from a boring in the North Sea[7]. The sediment indicates freshwater conditions at a relative sea level of about -40 m, which we adjust to -23 ± 3 m based upon the subsidence estimates of Kooi et al.[12]. The model, however, places sea level at -13.6 ± 5.7 m. This result suggests that the North Sea in the region of this boring is subsiding faster than the estimates.

Third, the model identifies as a marginal outlier a terrace from South Point, Barbados, (terrace T-5b)[21], which has a modern elevation of 41.5 ± 1.7 m and an uplift-corrected paleo-sea level interpretation of 8.1 ± 4.6 m. The model assigns it an elevation of 2.6 ± 3.3 m. Given the high uplift rate in Barbados, this degree of mismatch is unsurprising.

Finally, the model identifies six time points from the Red Sea curve between 124.3 and 118.1 ka as

outliers. At three time points (all with nominal ages between 123.4 and 123.1 ka), the model identifies the data points as overestimates; at three other time points (nominally 124.3, 121.9, and 118.1 ka) the model identifies the data points as underestimates.

The four data points for which the age measurements were marginal outliers were a single coral observation from -1.15 m in the Turtle Bay borehole from East Wallabi Island, Houtman-Abrohlos Islands[23], a 3 m reef terrace from La Digue Island in the Seychelles[44], a 2.4 m exposed reef from Rottnest Island, Australia[39], and a poorly dated 8 m erosional terrace from Aldabra[45]. All four of these identifications are quite marginal; given the uncertainties surrounding the age model, we do not place much stock in them. The Turtle Bay coral has a U-Th age of 129.5 ± 2.6 ka but a model age of 126.6 ka (67% range of 125.9 to 130.8 ka). The La Digue Island reef terrace has a U-Th age of 128.5 ± 3.7 ka but a model age of 125.5 ka (67% range of 124.6 to 130.1 ka). The Rottnest Island reef has a U-Th age of 126.1 ± 1.8 ka but a model age of 125.4 ka (67% range of 124.8 to 130.0 ka). Finally, we assigned the Aldabra terrace a stratigraphic age of 100 ± 35 ka; the model assigns it an age of 120.2 ka (67% range of 115.8 to 123.2 ka).

In addition to these outliers, prior to the primary analysis discussed in the text, we removed three data points that appeared incompatible with our assumed age model. All three points come from the Houtman-Abrohlos Islands[22,23]. The first, a coral at +0.6 m from Mangrove Island, had a reported age of 132.8 ± 0.9 ka. The second, corals from -4.3 m in a bore hole on Rat Island, had a reported age of 134.3 ± 1.3 ka. The third, corals from -3.3 m in a bore hole on Turtle Island, had a reported age of 132.5 ± 1.8 ka. None of the other observations in the database suggested sea levels so close to the modern values at such early ages, and these elevations were clearly incompatible with the oxygen isotope curve used as the basis for the prior. We therefore interpreted these samples as misdated and did not include them.

Need for more data. The ratio of the posterior to prior model covariance is small when the model successfully improves our initial state of knowledge by incorporating the data. Where it remains large, more, or better data, is needed to improve the model. Inasmuch as local data can improve resolution locally, we

can take the value of this ratio to indicate a "data need." While resolution is not a strictly local concept, we define the "data need index" (Figure S10) as the mean of the ratio of the posterior variance to the prior variance over the time period between 114 and 129 ka and plot it over the globe. Because we are particularly interested in sea level near the highstand, we weight the mean by the probability that a sample time slice has global sea level greater than -10 m.

The highest data need is in the near-field and intermediate-field of the major ice sheets. Other areas of high need are fairly widespread along continental coasts. In the far-field of both Northern Hemisphere and Southern Hemisphere ice sheets, the coasts of East and Southeast Asia are notably lacking in the data collection. Unfortunately, acquiring high-precision Asian sea level data for the Last Interglacial will be complicated by the region's active neotectonics.

In compiling the LIG sea level database, we also found a number of regions where sea level indicators require further investigation. For instance, although Britain is on a tectonically stable passive margin, erosional terraces appear to get progressively older with increasing elevation. Westaway et al.[24] estimated Pleistocene uplift rates in the vicinity of the Solent river system range of ~ 10 m/ky. The causes of this uplift are uncertain, but might be linked to isostatic effects caused by erosional unroofing and the transport of sediment from continent to slope. A simple isostatic calculation indicates this method requires the removal of $\sim$50 m of sediment per 100 ky. Clayton[25] estimates that an average thickness of $\sim$145 m of sediment was removed from the land of the British Isles to the continental shelf during the last glaciation; this removal could therefore be a potential cause. Because the British Isles are in a crucial region to look for the sea-level fingerprint of Greenland melting, a better understanding of regional uplift would be extremely helpful.

Braithwaite[26] described numerous terraces in the coastal limestone of Kenya which range in elevation from -35 m to +20 m but lack good age constraints. These represent ready targets for modern dating techniques.

Supplementary References

1. Lighty, R. G., Macintyre, I. G. & Stuckenrath, R. Acropora palmata reef framework: A reliable indicator of sea level in the western Atlantic for the past 10,000 years. *Coral Reefs* **1**, 125–130 (1982).

2. Camoin, G. F., Ebren, P., Eisenhauer, A., Bard, E. & Faure, G. A 300,000-yr coral reef record of sea level changes, Mururoa atoll (Tuamotu archipelago, French Polynesia). *Palaeogeography, Palaeoclimatology, Palaeoecology* **175**, 325–341 (2001).

3. Lisiecki, L. E. & Raymo, M. E. A Pliocene-Pleistocene stack of 57 globally distributed benthic δ^{18}O records. *Paleoceanography* **20**, 1–17 (2005).

4. Scholz, D. & Mangini, A. How precise are U-series coral ages? *Geochimica et Cosmochimica Acta* **71**, 1935–1948 (2007).

5. Godwin-Austen, R. On the newer Tertiary deposits of the Sussex coast. *Quarterly Journal of the Geological Society* **12**, 4 (1856).

6. Rohling, E. J. *et al.* High rates of sea-level rise during the last interglacial period. *Nature Geoscience* **1**, 38–42 (2008).

7. Zagwijn, W. H. Sea-level changes in the Netherlands during the Eemian. *Geologie en Mijnbouw* **62**, 437–450 (1983).

8. Siddall, M. *et al.* Sea-level fluctuations during the last glacial cycle. *Nature* **423**, 853–858 (2003).

9. Thompson, W. G. & Goldstein, S. L. Open-system coral ages reveal persistent suborbital sea-level cycles. *Science* **308**, 401–405 (2005).

10. Zagwijn, W. H. An analysis of Eemian climate in Western and Central Europe. *Quaternary Science Reviews* **15**, 451–469 (1996).

11. van Leeuwen, R. J. W. *et al.* Stratigraphy and integrated facies analysis of the Saalian and Eemian sediments in the Amsterdam-Terminal borehole, the Netherlands. *Geologie en Mijnbouw* **79**, 161–196 (2000).

12. Kooi, H., Johnston, P., Lambeck, K., Smither, C. & Molendijk, R. Geological causes of recent (100 yr) vertical land movement in the Netherlands. *Tectonophysics* **299**, 297–316 (1998).

13. Rasmussen, C. & Williams, C. *Gaussian processes for machine learning* (MIT Press, Cambridge, MA, 2006).

14. Press, W. H., Teukolsky, S. A., Vetterling, W. T. & Flannery, B. P. *Numerical Recipes: The Art of Scientific Computing* (Cambridge University Press, 2007), third edn.

15. Peltier, W. R. Global glacial isostasy and the surface of the ice-age Earth: The ICE-5G (VM2) model and GRACE. *Annual Review of Earth and Planetary Sciences* **32**, 111–149 (2004).

16. Bintanja, R., van de Wal, R. S. W. & Oerlemans, J. Modelled atmospheric temperatures and global sea levels over the past million years. *Nature* **437**, 125–128 (2005).

17. Mitrovica, J. X. & Milne, G. A. On post-glacial sea level: I. General theory. *Geophysical Journal International* **154**, 253–267 (2003).

18. Meehl, G. A. *et al.* Global climate projections. In *Climate Change 2007: The Physical Science Basis*, chap. 10, 747–845 (Cambridge University Press, Cambridge, UK, 2007).

19. Hastings, W. K. Monte Carlo sampling methods using Markov chains and their applications. *Biometrika* **57**, 97–109 (1970).

20. Hearty, P. J., Hollin, J. T., Neumann, A. C., O'Leary, M. J. & McCulloch, M. Global sea-level fluctuations during the Last Interglaciation (MIS 5e). *Quaternary Science Reviews* **26**, 2090–2112 (2007).

21. Schellmann, G. & Radtke, U. A revised morpho- and chronostratigraphy of the Late and Middle Pleistocene coral reef terraces on Southern Barbados (West Indies). *Earth-Science Reviews* **64**, 157–187 (2004).

22. Zhu, Z. R. *et al.* High-precision U-series dating of Last Interglacial events by mass spectrometry: Houtman Abrolhos Islands, western Australia. *Earth and Planetary Science Letters* **118**, 281–293 (1993).

23. Eisenhauer, A., Zhu, Z., Collins, L., Wyrwoll, K. & Eichstätter, R. The Last Interglacial sea level change: new evidence from the Abrolhos islands, West Australia. *International Journal of Earth Sciences* **85**, 606–614 (1996).

24. Westaway, R., Bridgland, D. & White, M. The Quaternary uplift history of central southern England: evidence from the terraces of the Solent River system and nearby raised beaches. *Quaternary Science Reviews* **25**, 2212–2250 (2006).

25. Clayton, K. Quantification of the impact of glacial erosion on the British Isles. *Transactions of the Institute of British Geographers* **21**, 124–140 (1996).

26. Braithwaite, C. J. R. Depositional history of the late Pleistocene limestones of the Kenya coast. *Journal of the Geological Society, London* **141**, 685–699 (1984).

27. Allen, J. R. L. Interglacial high-tide coasts in the Bristol Channel and Severn Estuary, southwest Britain: a comparison for the Ipswichian and Holocene. *Journal of Quaternary Science* **17**, 69–76 (2002).

28. Keen, D. H., Harmon, R. S. & Andrews, J. T. U series and amino acid dates from Jersey. *Nature* **289**, 162–164 (1981).

29. Bates, M. R., Keen, D. H. & Lautridou, J.-P. Pleistocene marine and periglacial deposits of the English Channel. *Journal of Quaternary Science* **18**, 319–337 (2003).

30. Giresse, P., Barusseau, J. P., Causse, C. & Diouf, B. Successions of sea-level changes during the Pleistocene in Mauritania and Senegal distinguished by sedimentary facies study and U/Th dating. *Marine Geology* **170**, 123–139 (2000).

31. Stea, R. R., Piper, D. J. W., Fader, G. B. J. & Boyd, R. Wisconsinan glacial and sea-level history of Maritime Canada and the adjacent continental shelf: A correlation of land and sea events. *GSA Bulletin* **110**, 821–845 (1998).

32. Stea, R., Fader, G., Scott, D. & Wu, P. Glaciation and relative sea-level change in Maritime Canada. In Weddle, T. K. & Retelle, M. J. (eds.) *Deglacial history and Relative Sea-Level Changes, Northern New England and Adjacent Canada*, no. 351 in Special Paper, 35–50 (Geological Society of America, Boulder, Colorado, 2001).

33. Cronin, T. M., Szabo, B. J., Ager, T. A., Hazel, J. E. & Owens, J. P. Quaternary climates and sea levels of the U.S. Atlantic Coastal Plain. *Science* **211**, 233–240 (1981).

34. Muhs, D. R., Simmons, K. R. & Steinke, B. Timing and warmth of the Last Interglacial period: new U-series evidence from Hawaii and Bermuda and a new fossil compilation for North America. *Quaternary Science Reviews* **21**, 1355–1383 (2002).

35. Chen, J. H., Curran, H. A., White, B. & Wasserburg, G. J. Precise chronology of the last interglacial period: ^{234}U-^{230}Th data from fossil coral reefs in the Bahamas. *Geological Society of America Bulletin* **103**, 82–97 (1991).

36. Tomazelli, L. J. & Dillenburg, S. R. Sedimentary facies and stratigraphy of a last interglacial coastal barrier in south Brazil. *Marine Geology* **244**, 33–45 (2007).

37. Rostami, K., Peltier, W. R. & Mangini, A. Quaternary marine terraces, sea-level changes and uplift

history of Patagonia, Argentina: comparisons with predictions of the ICE-4G (VM2) model of the global process of glacial isostatic adjustment. *Quaternary Science Reviews* **19**, 1495–1525 (2000).

38. Murray-Wallace, C. & Belperio, A. P. The Last Interglacial shoreline in Australia – a review. *Quaternary Science Reviews* **10**, 441–461 (1991).

39. Stirling, C. H., Esat, T. M., McCulloch, M. T. & Lambeck, K. High-precision U-series dating of corals from Western Australia and implications for the timing and duration of the Last Interglacial. *Earth and Planetary Science Letters* **135**, 115–130 (1995).

40. Stirling, C. H., Esat, T. M., Lambeck, K. & McCulloch, M. T. Timing and duration of the Last Interglacial: evidence for a restricted interval of widespread coral reef growth. *Earth and Planetary Science Letters* **160**, 745–762 (1998).

41. Hobday, D. K. Quaternary sedimentation and development of the lagoonal complex, Lake St. Lucia, Zululand. *Annals of the South African Museum* **71**, 93–113 (1975).

42. Ramsay, P. J. & Cooper, J. A. G. Late Quaternary sea-level change in South Africa. *Quaternary Research* **57**, 82–90 (2002).

43. Woodroffe, C. D. Late Quaternary sea-level highstands in the central and eastern Indian Ocean: A review. *Global and Planetary Change* **49**, 121–138 (2005).

44. Israelson, C. & Wohlfarth, B. Timing of the Last-Interglacial high sea level on the Seychelles Islands, Indian Ocean. *Quaternary Research* **51**, 306–316 (1999).

45. Braithwaite, C. J. R., Taylor, J. D. & Kennedy, W. J. The evolution of an atoll: The depositional and erosional history of Aldabra. *Philosophical Transactions of the Royal Society of London Series B* **266**, 307–340 (1973).

46. Brigham-Grette, J. & Hopkins, D. M. Emergent marine record and paleoclimate of the Last Interglaciation along the northwest Alaskan coast. *Quaternary Research* **43**, 159–173 (1995).

47. Gualtieri, L., Vartanyan, S., Brigham-Grette, J. & Anderson, P. M. Pleistocene raised marine deposits on Wrangel Island, northeast Siberia and implications for the presence of an East Siberian ice sheet. *Quaternary Research* **59**, 399–410 (2003).

48. Forman, S. L. & Miller, G. H. Time-dependent soil morphologies and pedogenic processes on raised beaches, Bröggerhalvöya, Spitsbergen, Svalbard Archipelago. *Arctic and Alpine Research* **16**, 381–394 (1984).

49. Andersson, T., Forman, S. J., Ingólfsson, Ó. & Manley, W. F. Late Quaternary environmental history of central Prins Karls Forland, western Svalbard. *Boreas* **28**, 292–307 (1999).

50. Landvik, J. Y., Lysa, A., Funder, S. & Kelly, M. The Eemian and Weicheselian stratigraphy of the Langelandslev area, Jameson Land, East Greenland. *Boreas* **23** (1994).

51. Vosgreau, H. *et al.* Paleoenvironments and changes in relative sea level during the last interglaciation at Langelandslev, Jameson Land, East Greenland. *Boreas* **23**, 398–411 (1994).

52. Gardner, N., Hall, B. & Wehmiller, J. Pre-Holocene raised beaches at Cape Ross, Southern Victoria Land, Antarctica. *Marine Geology* **229**, 273–284 (2006).

Supplementary Tables

Table S1: **Sites, Number, and Types of Sea Level Indicators in the LIG Database**

Site	# Observations	Type	Reference
Northeastern Atlantic Ocean and Mediterranean Sea			
Southern England	2	erosional	24
Bristol Channel, Britain	1	erosional	27
Belle Hogue Cave, Jersey	1	erosinal	28
Port-Racine Beach, France	1	erosional	29
The Netherlands	8	facies	7
Hergla South, Tunisia	2	facies	20
Quaternary Basin, Mauretania	2	facies	30
Northwestern Atlantic Ocean and Carribean Sea			
Cape George, Nova Scotia	1	erosional	31,32
Mark Clark, South Carolina	1	facies	33
Grape Bay, Bermuda	2	facies	20,34
San Salvador Island, Bahamas	3	reef	35
Great Inagua Island, Bahamas	3	reef; erosional	35
Abaco Island, Bahamas	3	reef; erosional	20
Southern Barbados	8	reef	21
Southwestern Atlantic Ocean			
Rio Grande do Sol coastal plain, Brazil	1	facies	36
Camarones, Patagonia, Argentina	1	erosional	37
Pacific Ocean			
Oahu, Hawaii	3	reef; corals; facies	20,34
Mururoa Atoll	1	corals	2
Australia			
Eyre Peninsula	1	facies	38
Rottnest Island	1	reef	20,39
Minim Cove	1	facies	20
Cape Range	2	reef	40

Continued on Next Page…

Table S1: **Sites, Number, and Types of Sea Level Indicators in the LIG Database**

Site	# Observations	Type	Reference
Houtman Abrohlos Islands	8†	reef; facies; corals	22,23
Indian Ocean and Red Sea			
Red Sea	30	isotopic	6
KwaZulu-Natal, South Africa	3	erosional; facies	41,42
Eastern Cape, South Africa	1	erosional	42
Maldives Archipelago	1	facies	43
La Digue Island, Seychelles	2	reef	44
Aldabra Atoll, Seychelles	3	corals; facies	45
Polar regions			
Northern and Western Alaska	3	facies	46
Wrangel Island, Siberia	1	facies	47
Western Spitsbergen	3	erosional	48,49
Scoresby Sund, Greenland	3	facies	50,51
Cape Ross, Antarctica	1	erosional	52

† Three observations removed due to mismatch with age model.

Table S2: Summary statistics for different Gaussian taper widths and data subsets.

		Max. Median GSL		GSL exceed. levels (m)			Rate exceed. levels (m/ky)		
Taper (ky)	Subset	Age (ky)	Level (m)	95%	67%	33%	95%	67%	33%
3	Std.	124	7.0 ± 1.4	6.6	8.0	9.4	5.6	7.4	9.2
2	Std.	124	6.9 ± 1.3	6.3	7.6	8.7	5.7	7.5	9.1
4	Std.	124	7.3 ± 1.3	6.5	7.8	8.9	5.7	7.5	9.1
-	Std.	131	13.0 ± 15.2	6.7	8.5	12.6	6.0	8.1	10.9
3	Full	124	7.0 ± 1.4	6.6	8.1	10.1	5.8	8.0	10.7
3	-Cor.	123	7.2 ± 1.8	5.8	7.5	8.9	5.8	7.9	9.6
3	-Eros.	124	6.8 ± 1.3	5.9	7.2	8.4	5.3	7.3	9.1
3	-Fac.	124	7.7 ± 1.4	6.3	7.7	8.8	5.5	7.3	8.9
3	-Iso.	127	6.8 ± 3.2	7.0	8.7	10.5	3.9	6.5	9.5
3	+Cor.	128	8.7 ± 2.0	6.2	8.3	10.0	-0.1	4.0	8.0
3	+Ero.	128	6.4 ± 7.2	-0.3	3.9	6.8	-8.0	1.4	6.3
3	+Fac.	119	6.7 ± 2.5	6.1	8.0	9.7	1.2	4.7	7.3

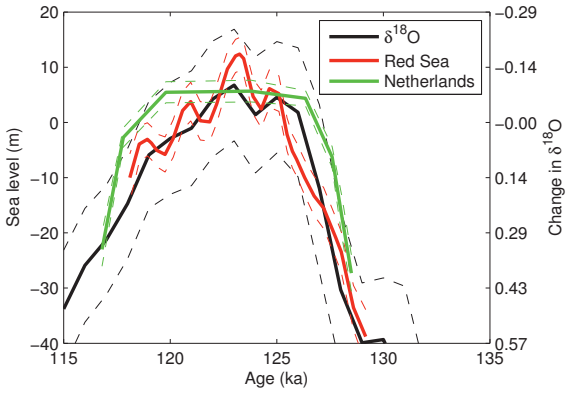

Figure S1: The oxygen isotope-based estimate of global sea level (black) and local sea level curves from the Red Sea (red) and the Netherlands (green). Dashed lines show 1σ confidence intervals in sea level. The initial best alignment of the three curves is shown. On the right axis, the black curve also shows the deviation of the underlying global oxygen isotope stack from its present-day value of $3.23 \pm 0.03‰$ (PDB)[3].

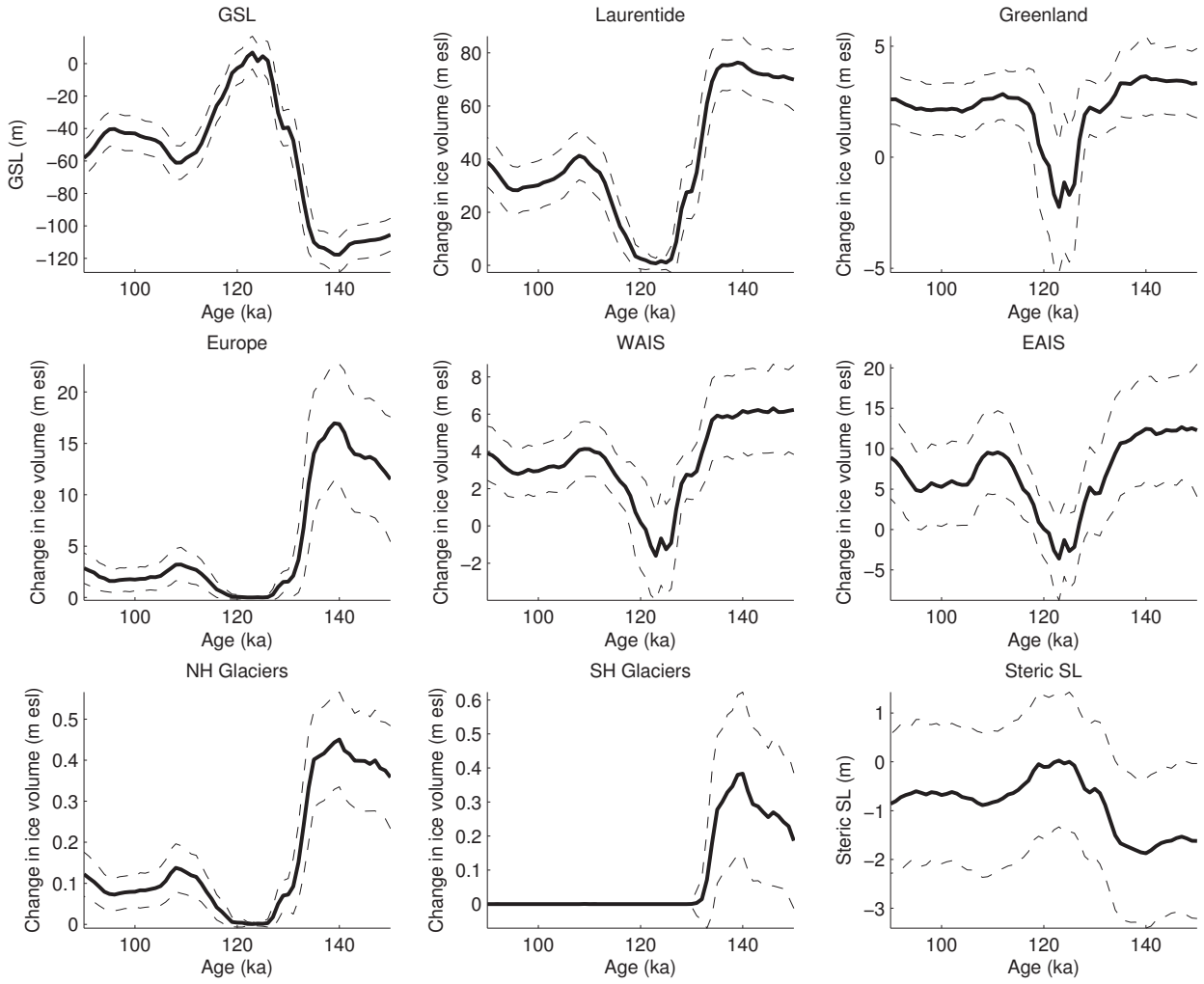

Figure S2: Distributions of global sea level, changes in ice sheet volumes, and steric sea level in the 250 alternative histories used to construct the prior distribution. Dashed lines show 1σ ranges.

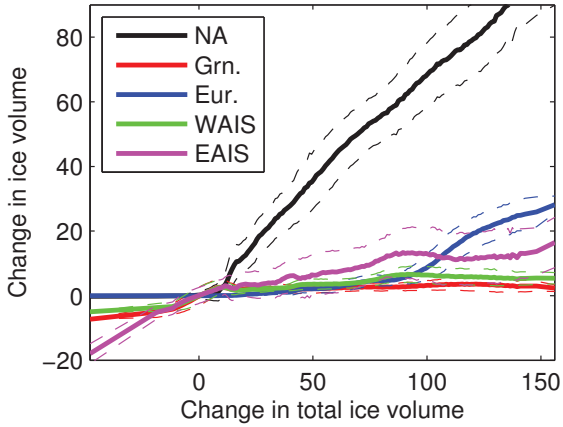

Figure S3: Mean and standard deviation of the change in volume of each ice sheet as a function of change in total ice volume. Dashed lines show 1σ ranges.

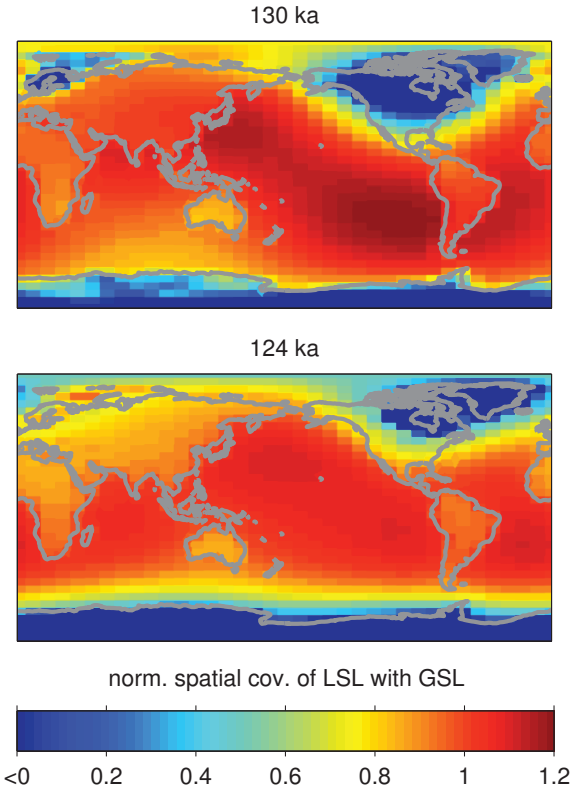

Figure S4: The spatial covariance of local sea level with global sea level at 130 ka and 124 ka, normalized to the contemporaneous variance of global sea level (σ_{GSL} = 11.6 m at 130 ka and 10.5 m at 124 ka).

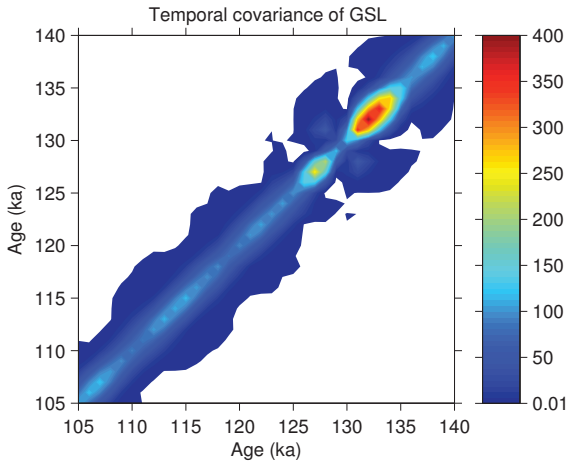

Figure S5: The covariance of GSL over time as employed in the main analysis (with a 3 ky Gaussian taper).

In the unshaded areas, the covariance is less than 0.01.

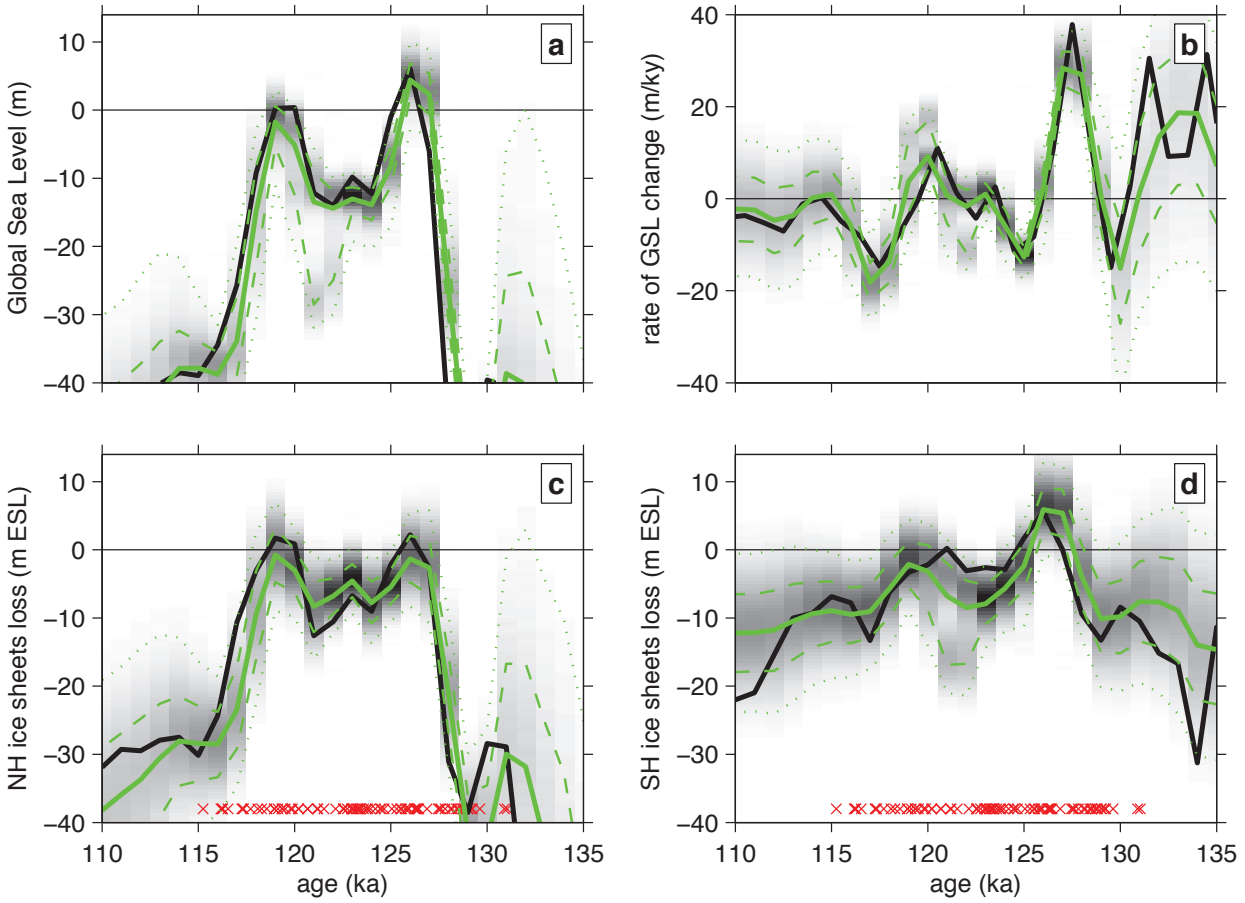

Figure S6: Reconstructed (a) GSL, (b) GSL rate, (c) NH ice volume and (d) SH ice volume for a synthetic sea level history. The heavy green lines mark the median projections based on the statistical analysis of pseudo-proxies, while the dashed lines mark the 16th and 84th percentiles, and dotted lines mark the 2.5th and 97.5th percentiles. The heavy black lines mark the "true" values.

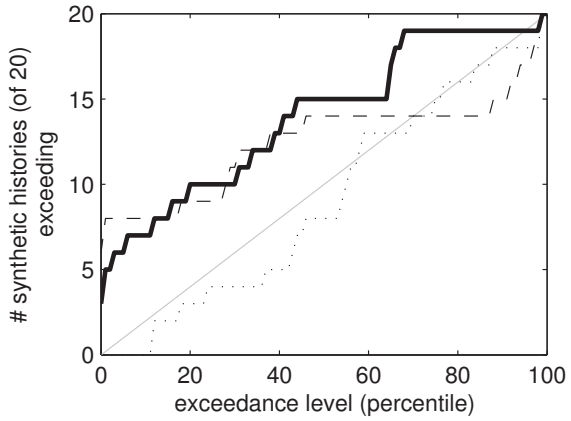

Figure S7: Number of synthetic histories (out of 20) in which the "true" maximum value exceed a given exceedance value. The heavy solid line shows global sea level rise, the dashed line shows the 1000-year average rate of change of global sea level when global sea level is at or above -10 m, and the dotted line shows ice loss in the hemisphere with the least ice loss. The grey line indicates the expected values if the distribution of synthetic histories conformed precisely to the distribution specified by the exceedance values.

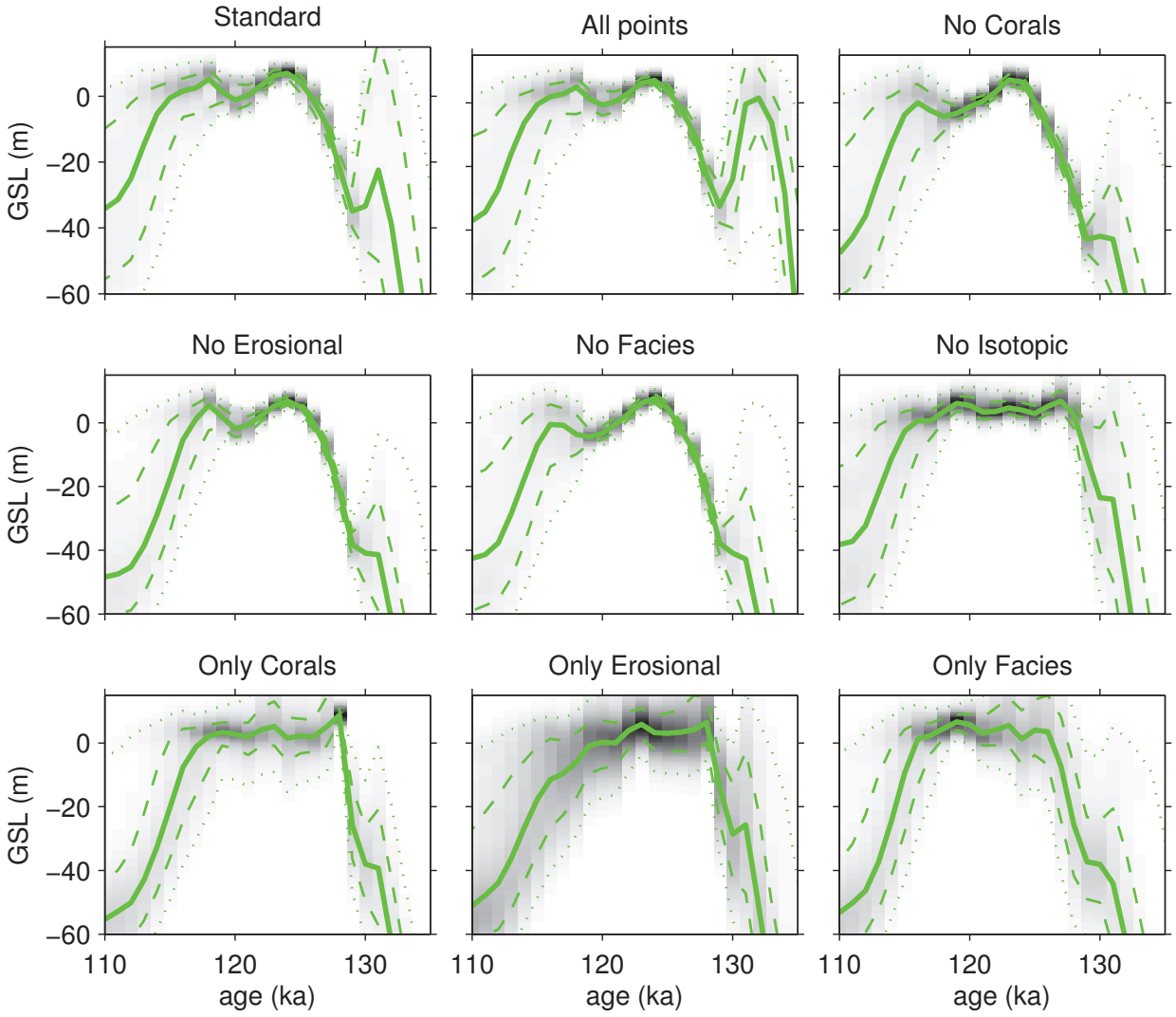

Figure S8: Projections of GSL using different subsets of the data. The "standard" subset excludes three data points from the Houtman Abrohlos islands that are inconsistent with the age model, while the "full subset" includes them. The remaining seven subsets either exclude or consist only of measurements based on corals, erosional features, facies interpretations, or the Red Sea isotope curve. The heavy lines mark the median projections, dashed lines mark the 16th and 84th percentiles, and dotted lines mark the 2.5th and 97.5th percentiles. Summary statistics are provided in Table S2.

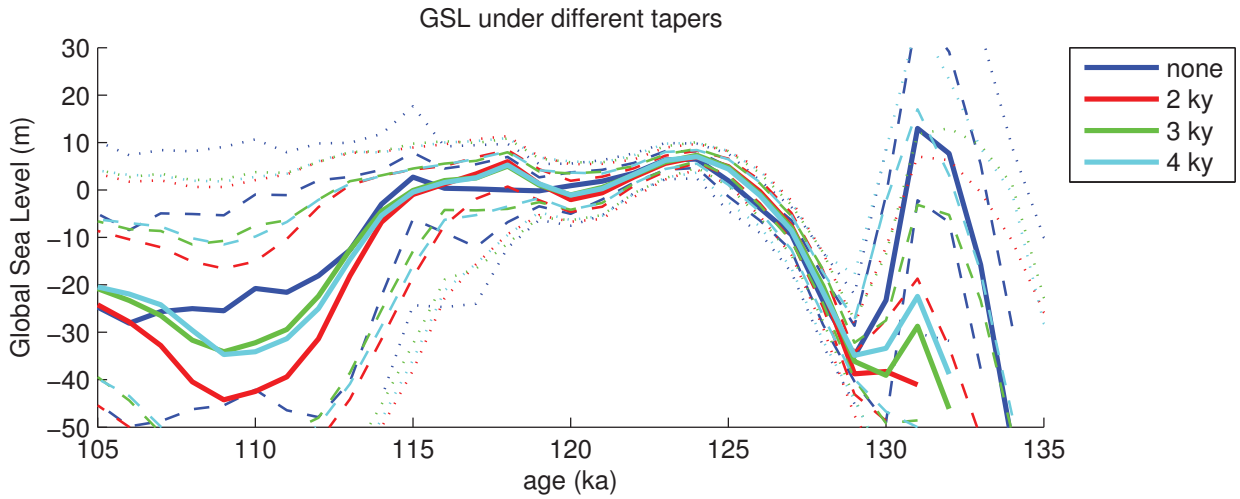

Figure S9: GSL projections using different width Gaussian temporal taper functions in the covariance function. Summary statistics are provided in Table S2. The heavy lines mark the median projections, dashed lines mark the 16th and 84th percentiles, and dotted lines mark the 2.5th and 97.5th percentiles.]

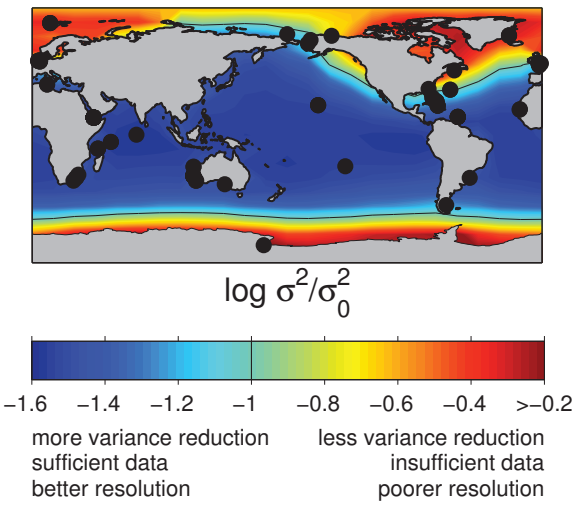

Figure S10: Map of the data need index. We calculate this index by averaging the ratio of the posterior variance to the prior variance over the time period between 114 and 129 ka.